



OPEN ACCESS

EDITED BY

Thomas FitzGerald,
University of Massachusetts Boston,
United States

REVIEWED BY

A Nasser Khalifeh,
University of Massachusetts Medical
School, United States
Fenghong Liu,
UMass Memorial Medical Center,
United States

*CORRESPONDENCE

Linda Eliasson
lindaeli@kth.se

SPECIALTY SECTION

This article was submitted to
Radiation Oncology,
a section of the journal
Frontiers in Oncology

RECEIVED 23 February 2022

ACCEPTED 05 July 2022

PUBLISHED 02 August 2022

CITATION

Eliasson L, Lillhök J, Bäck T, Billnert-
Maróti R, Dasu A and Liszka M (2022)
Range-shifter effects on the stray field
in proton therapy measured with the
variance-covariance method.
Front. Oncol. 12:882230.
doi: 10.3389/fonc.2022.882230

COPYRIGHT

© 2022 Eliasson, Lillhök, Bäck, Billnert-
Maróti, Dasu and Liszka. This is an
open-access article distributed under
the terms of the [Creative Commons
Attribution License \(CC BY\)](https://creativecommons.org/licenses/by/4.0/). The use,
distribution or reproduction in other
forums is permitted, provided the
original author(s) and the copyright
owner(s) are credited and that the
original publication in this journal is
cited, in accordance with accepted
academic practice. No use,
distribution or reproduction is
permitted which does not comply with
these terms.

Range-shifter effects on the stray field in proton therapy measured with the variance-covariance method

Linda Eliasson^{1*}, Jan Lillhök², Torbjörn Bäck¹,
Robert Billnert-Maróti², Alexandru Dasu³
and Malgorzata Liszka⁴

¹Department of Physics, KTH, Stockholm, Sweden, ²The Swedish Radiation Safety Authority, Solna, Sweden, ³Medical Radiation Sciences, Department of Immunology, Genetics and Pathology, Uppsala University, Uppsala, Sweden, ⁴The Skandion Clinic, Uppsala, Sweden

Measurements in the stray radiation field from a proton therapy pencil beam at energies 70 and 146 MeV were performed using microdosimetric tissue-equivalent proportional counters (TEPCs). The detector volumes were filled with a propane-based tissue-equivalent gas at low pressure simulating a mean chord length of 2 μm in tissue. Investigations were performed with and without a beam range shifter, and with different air gaps between the range shifter and a solid water phantom. The absorbed dose, the dose-mean lineal energy, and the dose equivalent were determined for different detector positions using the variance-covariance method. The influence from beam energy, detector- and range-shifter positions on absorbed dose, LET, and dose equivalent were investigated. Monte Carlo simulations of the fluence, detector response, and absorbed dose contribution from different particles were performed with MCNP 6.2. The simulated dose response for protons, neutrons, and photons were compared with, and showed good agreement with, previously published experimental data. The simulations also showed that the TEPC absorbed dose agrees well with the ambient absorbed dose for neutron energies above 20 MeV. The results illustrate that changes in both dose and LET variations in the stray radiation field can be identified from TEPC measurements using the variance-covariance method. The results are in line with the changes seen in the simulated relative dose contributions from different particles associated with different proton energies and range-shifter settings. It is shown that the proton contribution scattered directly from the range shifter dominates in some situations, and although the LET of the radiation is decreased, the ambient dose equivalent is increased up to a factor of 3.

KEYWORDS

LET, TEPC, variance-covariance method, dose-mean lineal energy, out-of-field dose, dose equivalent, proton therapy, pencil beam

1 Introduction

Compared to conventional photon therapy, proton therapy has the potential of reducing exposure and radiation risks outside the target volume (1). Nevertheless, there is still a concern that stray radiation can increase secondary cancer risks. In an ongoing task within EURADOS working group 9, the relation between the most critical treatment parameters and the out-of-field neutron doses is therefore investigated. The outcome will hopefully be a first step toward a tool for medical physicists to estimate the neutron doses directly from the treatment parameters. Simulations and results from experimental campaigns are further described in Van Hoey et al. (2).

In the EURADOS WG9 campaign, the quantity used for comparison was the neutron ambient dose equivalent, $H_n^*(10)$ (3). During the measurement campaign at the Skandion Clinic in 2019, the Swedish Radiation Safety Authority contributed with three instruments, a Berthold LB6411 neutron monitor and two tissue-equivalent proportional counters (TEPCs), further called the Sievert detectors. TEPCs can detect and separate both high- and low-LET components, which makes them suitable for mixed radiation fields.

With varying different treatment settings in the experiment described by Van Hoey et al. (2), $H_n^*(10)$ was measured with different detectors in various positions around a solid water phantom. In one position, a significant increase in absorbed dose was measured with the Sievert detector when the range shifter was inserted. This increase was not supported by simulations or measurements performed by neutron monitors in the vicinity of the same position. A hypothesis was that scattered protons from the range shifter contributed to the absorbed dose in positions that were less shielded by the phantom.

Prior to the campaign described by Van Hoey et al. (2), several measurements as well as simulation comparisons of out-of-field doses have been conducted. It is, e.g., well known that the stray neutron fields are characterised by a thermal and high-energy component (4, 5). Range shifters and their effect on the stray neutron field have also been studied, and alternative methods to scan shallow tumours have been reported to decrease the high-LET contribution to the dose (6). However, proton scattering from the range shifter is rarely considered.

The ambient dose equivalent, $H^*(10)$, is defined in terms of the dose equivalent $H = D \cdot Q(L)$ at 10-mm depth in the ICRU sphere in an expanded and aligned radiation field (7, 8). Here D is the absorbed dose in tissue and $Q(L)$ is a quality factor that depends on the unrestricted linear energy transfer (LET) of charged particles in water. The linear energy transfer can be estimated by the lineal energy, y , measured with TEPCs simulating a tissue volume in the micrometre range (9). The distribution of y -values hence corresponds to the LET distribution of the radiation field. A change in this

distribution, or, e.g., the dose-mean lineal energy \bar{y}_D , reflects a change in the LET of the radiation field.

In addition to microdosimetric single-event measurements, the variance-covariance method (10) has been used for radiation protection applications in mixed fields. Lillhök et al. measured differences in the stray radiation fields between photon and proton therapy (11). Several cosmic radiation measurements have been performed, where the variance and variance-covariance methods have been compared with other methods (12, 13) and with several instruments (14). The method has also successfully been used in mixed workplace fields with photons and neutrons and strongly pulsed stray radiation fields from accelerators (15, 16). Single-event measurements are limited in high-intensity fields due to pile-up which can be the case, e.g., in a therapeutic beam. As described in Lillhök et al. (13), TEPCs used for both single- and multi-event measurements showed good agreement in the mixed field onboard an aircraft and showed that it can be used as a complementary method in mixed fields.

In the investigation presented in this article, measurements complementary to the EURADOS 2019 campaign (2) were performed at the Skandion Clinic, aiming to study the dose contribution and LET of the stray radiation component from the range shifter using two Sievert detectors, which as previously described are multi-event TEPCs. The absorbed dose and dose-mean lineal energy were measured using the variance-covariance method. A phantom was placed in the same position as in the 2019 campaign and irradiated with two different proton beam energies for a variety of different range-shifter settings. Measurements were also performed without a phantom to quantify the range-shifter component directly. The detector absorbed dose responses for neutrons, protons, photons, and electrons were simulated using MCNP 6.2. These response functions were used together with simulated fluence distributions at the detector positions to evaluate the relative absorbed dose contributions from different radiation field components.

2 Method

2.1 Experimental method and equipment

The Sievert detectors are made of A-150 plastic, contained in a 2-mm-thick aluminum container and filled with propane-based tissue-equivalent gas (17) to a pressure of 1.37 kPa, corresponding to a simulated tissue volume with a mean chord length of 1.88 μm . The instruments are cylindrical with diameters and heights equal to 11.54 cm and with an A150-plastic wall of thickness 5 mm. The electric charge generated in each detector is measured using a 1-nF feedback capacitor, where the voltage over the capacitor is measured 10 times per second with a 24-bit analogue-to-digital converter (ADS

1210U). One bit is used for polarity and the other 23 bits for dividing the maximum capacitor voltage of 5 V into steps of 0.6 μ V. The electronic noise is dominated by the 0.6- μ V (rms) contribution from the analogue-to-digital-converter (18). The absorbed dose to the detector gas during the integrated time is determined by

$$D_{det} = \frac{qW}{Mm_{det}}, \quad (1)$$

where q is the electric charge collected during the integration time, W is the mean energy expended to create an ion pair (in energy per charge), M is the gas multiplication factor, and m_{det} is the detector gas mass. The dose-mean lineal energy is calculated using the variance-covariance method,

$$\bar{y}_D = \frac{m_{det}(V_{rel} - C_{rel})}{\bar{l}_\mu} \bar{D}_{det}, \quad (2)$$

where V_{rel} is the relative variance in the absorbed dose during the repeated charge, C_{rel} is the relative covariance between two detectors experiencing the same field, \bar{l}_μ is the mean chord length for the simulated tissue, and \bar{D}_{det} is the average dose over repeated integration times (10). In a time-varying radiation field, a covariance correction is usually determined using a second detector. However, in some situations the radiation field variations at the two detector positions are not necessarily synchronised in time. In such cases, a covariance correction can be obtained from the consecutive charge integrations. This method is further described in Eliasson et al. (article in progress) and was used in the measurements presented here.

In a mixed field, where several components contribute, the measured total \bar{y}_D value is given by a combination of the relative dose contributions and their dose-mean lineal energies. As an example, the case with three components can be written as

$$\bar{y}_D = d_\gamma \bar{y}_{D,\gamma} + d_n \bar{y}_{D,n} + d_p \bar{y}_{D,p}, \quad (3)$$

where d_i is the relative dose contribution for photons, neutrons, and protons, respectively. From the equation, it is clear that a change in any of the component contributions will be reflected as a change in the measured \bar{y}_D value. As previously mentioned, the dose-mean lineal energies for the radiation components are energy dependent and can be estimated by using their simulated fluence distributions for the stray field and a known response function determined in monoenergetic beams (18, 19). The simulated response function and comparisons with measurements are described in the following sections. While the $\bar{y}_{D,\gamma}$ value depends strongly on the neutron energy, it is in stray fields from proton therapy dominated by high-energy neutrons, giving a $\bar{y}_{D,n}$ value typically around 100 keV/ μ m (1, 2), while the $\bar{y}_{D,\gamma}$ value is typically around 1.5 keV/ μ m (2, 11). For the proton component, the $\bar{y}_{D,p}$ value for a 1- μ m-diameter spherical object in water is approximately in the range 2–6 keV/ μ m for proton energies between 10 and 100 MeV but increases

with decreasing energies. At 1 MeV, the $\bar{y}_{D,p}$ value is approximately 40 keV/ μ m (20). Moreover, Kyllönen et al. measured dose-mean lineal energies in proton beams between 68 and 174 MeV with the Sievert detectors and reported \bar{y}_D values between 6.2 and 7.3 keV/ μ m (21).

Just as for the resulting \bar{y}_D value, the W value depends on the radiation components. However, the W values of photons, neutrons, and protons [26.8, 31, and 28.2 eV (22)] do not differ as dramatically from each other as the dose-mean lineal energies. Previous simulations of the stray field from a proton beam reported that the relative dose distribution from neutrons varied from approximately 54% to 95%, giving a W value that varied between 28.9 and 30.7 eV (11). The addition of a proton component does not change the mean value significantly, so the same mean value as reported by Lillhök et al. (11) was used for all irradiations in this article as well, and the variations were handled in the uncertainty estimation.

The $H^*(10)$ values were estimated from a measured dose equivalent, H^* , using a first-order approximation for the quality factor,

$$H^* = DQ_D = D (a + b\bar{y}_D), \quad (4)$$

where $a = 0.73$ and $b = 0.17 \mu\text{m}/\text{keV}$. (19). For this article, only total H^* values were determined, but it is possible to estimate the H^* values for the high- and low-LET components by using the relative dose contribution for each radiation component and the respective \bar{y}_D value in Equation 3.

No calibration factors relating the detector readings to D^* (10) or $H^*(10)$ directly are used. The absorbed dose (Equation 1) and dose-mean lineal energy (Equation 2) in the tissue-equivalent detector material are derived from traceable measures of air pressure and electric charge, where the physical detector volume with uncertainties is assumed to be representative of the true charge collecting volume. For the dose-equivalent measurements based on Equation 4, the constants a and b have been optimised for a neutron beam with a broad energy spectrum (19).

2.2 Experimental setup

The experiment was conducted at the Skandion clinic, which has been in operation since 2015 and is the first centre for proton beam therapy in the Nordic countries and the only centre situated in Sweden. By optimising the dose delivery to the target volume, the clinic can treat patients with tumours close to vital organs, reducing both the risk for secondary cancer and long-term side effects¹.

The proton beam at the facility is an IBA pencil beam and delivers protons with energies between 60 and 226 MeV (23–25).

¹ <https://skandionkliniken.se/en/>

A schematic illustration to scale and a photo of the setup are seen in Figures 1, 2. To better investigate the differences between range-shifter settings, only single-spot measurements were conducted, using a pristine beam. The detector positions A1 and C1 were similar to positions A and C in the 2019 campaign (2), while A3 and C3 were 10 cm further down the beam line. During the measurements, two detectors were used, where one detector was placed in any of the positions on the A side (A1 or A3) and the other was placed in the corresponding position on the C side (C1 or C3). The proton current was set to the same value, 0.6 nA, for all irradiations. A solid water (polystyrene) phantom of density 1.03 g/cm^3 , height and width equal to 30 cm, and length 60 cm was placed with its centre shifted 15 cm from the beam line. The range shifter is made of Lexan (polycarbonate) with a thickness of 3.11 cm and density of 1.20 g/cm^3 . Measurements were performed without the range shifter and with the range shifter at different air gaps (AG) from the phantom wall. For irradiations performed without the phantom, a proton beam dump was positioned at the far wall. The beam dump is made of PMMA with density 1.18 g/cm^3 , height 32 cm, thickness 6.5 cm, and length 40 cm. A total of 32 irradiations were performed with two different detector positions, two different proton beam energies, and a number of different range-shifter settings.

2.3 Simulations

The absorbed dose response of the detector and the particle fluence distributions in the different measurement positions were simulated with MCNP version 6.2 (26) in order to support and extend the analysis of the measurement results.

The response function for protons, neutrons, photons, and electrons were combined with the respective fluence distributions to calculate the relative absorbed dose contribution from each particle type.

2.3.1 Absorbed dose response of the Sievert detector

The absorbed dose response was simulated using a detector model in vacuum as shown in Figure 3, exposed to a parallel beam of monoenergetic particles with a beam diameter of 40 cm. The detector was filled with propane-based tissue-equivalent gas to a density of $26.12 \text{ } \mu\text{g/cm}^3$, corresponding to a mean chord length of $2 \text{ } \mu\text{m}$ tissue. The detector geometry was modelled as described in Section 2.1.

Simulations were carried out for 10^{-10} – 10^4 -MeV neutrons, 1 – 10^4 -MeV protons, 10^{-2} – 10^4 -MeV photons, and 10^{-2} – 10^4 -MeV electrons, using LA150 data libraries. Primary and secondary particles (photons, electrons, neutrons, protons, alpha-particles, deuterium, tritium ^3He , and heavy ions) were transported in all volumes. The absorbed dose in the cylindrical detector gas volume was scored using the +F6 tally for total heating. The +F6 tally scores energy depositions from all particles and not only a specific particle type. A linear energy binning was used for all particles with 10 bins per decade for neutrons and 20 bins per decade for protons, photons, and electrons. The total heating, i.e., absorbed dose, was normalised to the particle fluence.

2.3.2 Fluence distribution at the measurement positions

The fluence simulations were performed for a simple geometry only including a range shifter, a phantom, and a beam dump. The range shifter was modelled with dimensions $3.11 \text{ cm} \times$

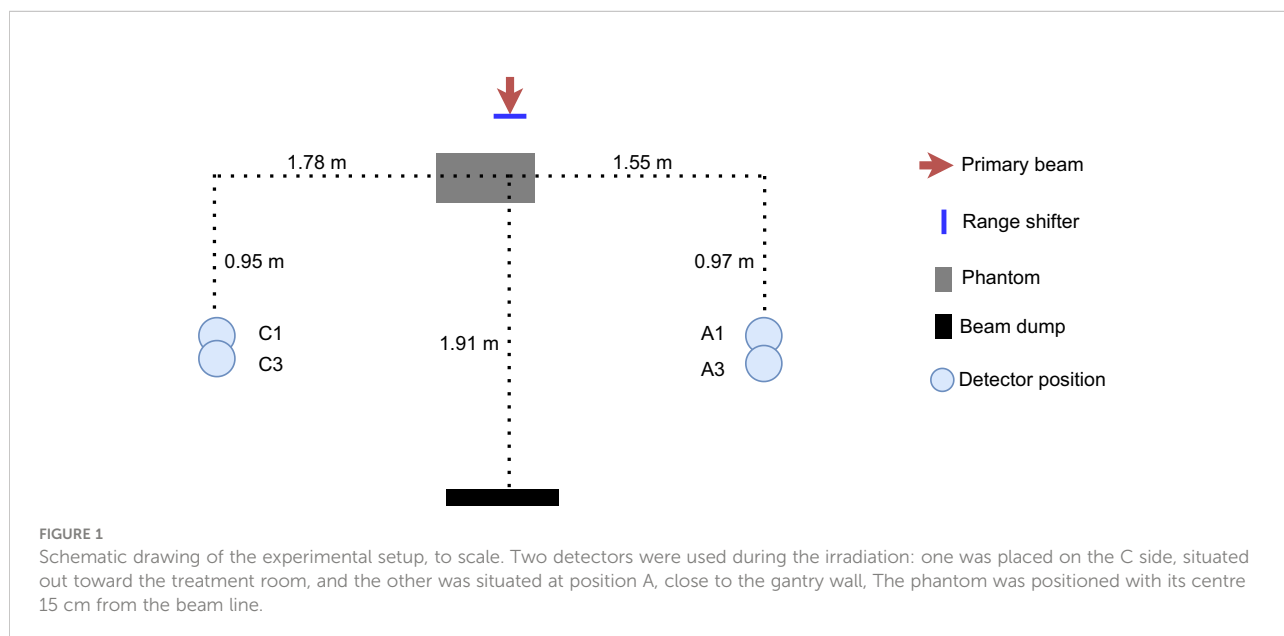




FIGURE 2

The experimental setup, with the two TEPCs in positions A and C. The C position is situated close to the gantry wall, while the A position in the foreground is facing the open treatment room.

15 cm × 15 cm, and the solid water phantom with dimensions as described in Section 2.2. Monoenergetic protons of energies 70 and 146 MeV in a circular and parallel beam of diameter 1 cm was transported through air to the range shifter positioned with different air gaps to the phantom. In order to quantify the effect of the range shifter, simulations were also performed with only the range shifter and no phantom, as well as only phantom with no range shifter. To further test the robustness of the relatively simple geometry, additional simulations were performed using a more comprehensive model with walls, floors, and the surrounding gantry structure (27).

The fluence distributions of neutrons, protons, photons, and electrons were first scored with tally F4 in spherical air volumes located in the same positions as the detectors in the measurements. Standard MCNP libraries were used, and photons, electrons, neutrons, protons, and alpha-particles were

transported in all volumes. A linear energy binning was used for all particles with 10 bins per decade for neutrons and 20 bins per decade for protons, photons, and electrons. The fluence was normalised to the number of initial protons.

2.3.3 The simulated absorbed dose

The fluence distributions and the detector response functions described above were used to estimate the relative dose contribution from neutrons, protons, photons, and electrons. The absorbed dose in the detector for particle type i is given by

$$D_{i,TEPC} = \sum_k d_{i,TEPC}(E_k) \Phi_i(E_k) \Delta E_k, \quad (5)$$

where $d_{i,TEPC}$ is the absorbed dose response per fluence of particle type i with energy E_k per energy bin, $\Phi(E_k)$ is the fluence

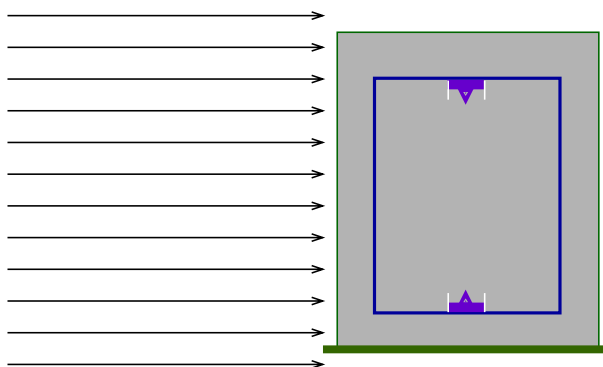


FIGURE 3

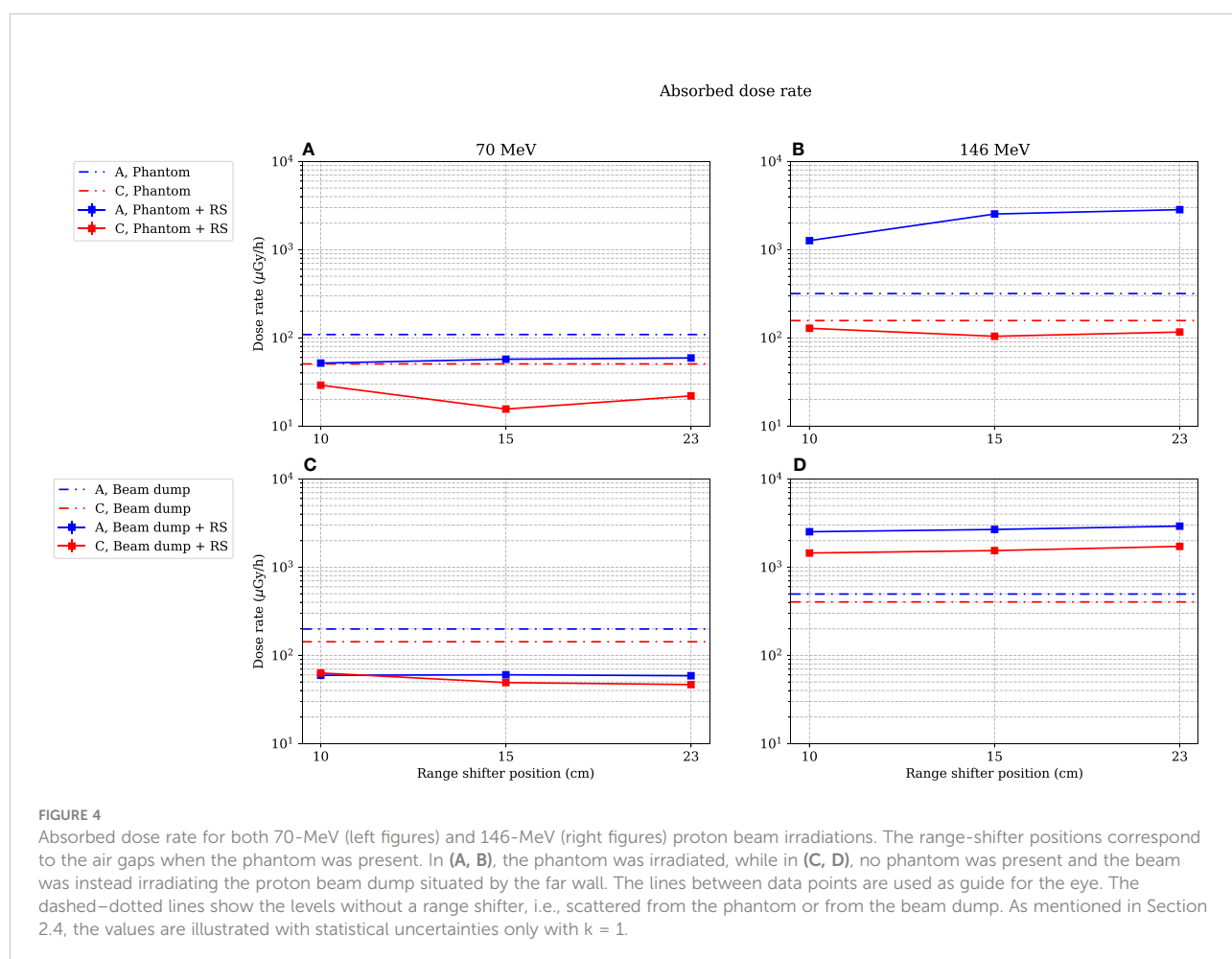
An illustration of the simulation geometry for the detector dose response simulations in MCNP 6.2. The cylindrical detector is confined in an aluminium container and exposed to monoenergetic beams.

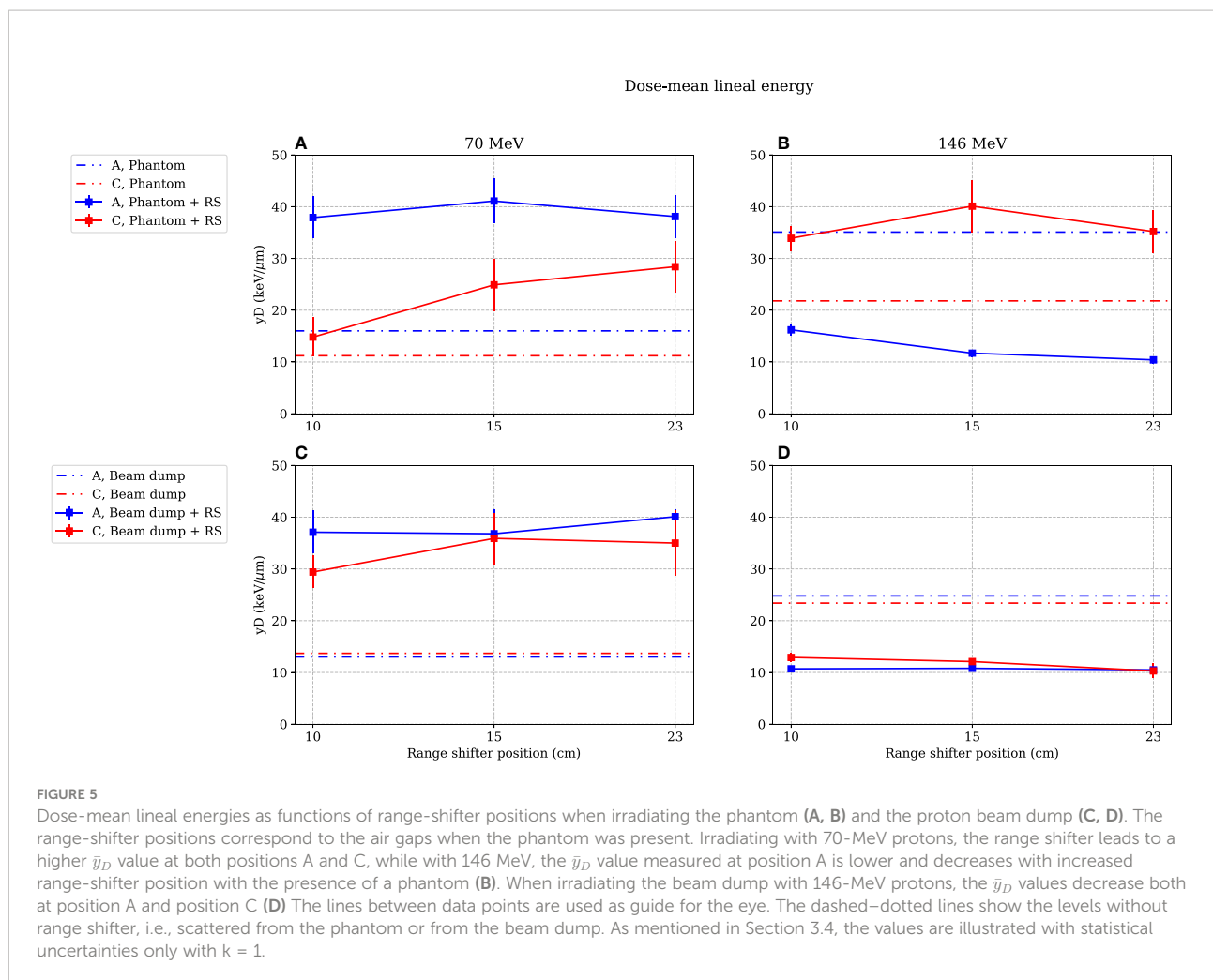
of particle type i with energy E_k per energy bin, and ΔE_k is the bin width with the average energy E_k in the fluence distribution. $D_{i,TEPC}$ is therefore summed over all energy bins and gives the total absorbed dose for one particle type i .

2.4 Uncertainties

The statistical uncertainties were estimated for the absorbed dose rate and for the dose equivalent using conventional error propagation. For the dose-mean lineal energy, the statistical uncertainty was obtained by splitting each data set into smaller subsets and calculating the standard deviation of the mean. In the results presented in Figures 4, 5 and 9, 10, and both tables below, only the statistical uncertainties are included, with coverage factor $k = 1$. The coverage factor was chosen to harmonise with the uncertainties presented in Van Hoey et al. (2). In addition, uncertainties of the gas pressure, detector volume and diameter, electric charge, W-value, gas multiplication, $H^*(10)$ response, and accelerator reference data need to be accounted for. The gas pressure has an uncertainty of

0.17%, estimated from calibrations of the pressure gauge at the Swedish National Metrology Laboratory for Pressure and Vacuum (RISE). The uncertainty in the generated electric charge is estimated to be 0.5% from cross-calibrations with a reference electrometer at the Swedish National Metrology Laboratory for Ionising Radiation. The uncertainties in the detector diameter and height are estimated to be 0.25% and 1.5%, respectively. Uncertainties in the effective charge collecting volume of the detector have not been taken into account, and the uncertainty in the volume was calculated directly from the dimensions. For the W value, the uncertainty was estimated to be 4%, which is the reported uncertainty for W_p (22). The other W values (W_n and W_γ) are reported with smaller uncertainties (22). The gas multiplication uncertainty (0.8%) was estimated from measurements in a calibrated ^{137}Cs field prior to and after the Skandion measurements. These above uncertainties give approximately 4% uncertainty contribution to add to the absorbed doses, the dose-mean lineal energies, and the dose equivalents. Since the Sievert instrument measures the absolute dose and variance between a series of 0.1-s charge collections, it is important that the proton current for each energy setting is





stable, while the absolute value of the proton current is less relevant. The dosimetry uncertainty budget from the Skandion Clinic ensures that the relative dose variation is within 2% (11). This was confirmed by the clinic's monitoring ionisation chambers.

The uncertainty in the $H^*(10)$ response of the detectors has not been included. This contribution varies with the relative contributions of the radiation components and has been reported to be about 15%–25% in typical mixed field applications (18).

The simulations are reported with statistical uncertainties with the coverage factor $k = 1$. Uncertainty contributions from, e.g., interaction cross sections and deviations between the simulated and real geometry, have not been taken into account.

3 Results

The differences in measured absorbed doses and dose-mean lineal energies between positions 1 and 3 were small, so only the

results from positions A1 and C1 are reported here. The positions are onward referred to as position A and position C. The absorbed dose, D , the dose-mean lineal energy, \bar{y}_D , and the dose equivalent, H^* , as functions of different range-shifter positions are presented for 70- and 146-MeV primary proton beams. The range-shifter settings 10, 15, and 23 cm correspond to air gaps of 10, 15, and 23 cm when the phantom is present and are in the figures referred to as AG. The experimental results are also presented in Tables 1, 2.

3.1 Measured absorbed dose as function of range-shifter position

Figure 4 shows the absorbed dose rate in positions A and C as a function of range-shifter position, both when irradiating a phantom (Figures 4A, B) and when irradiating the proton beam dump by the far wall (Figures 4C, D). The dotted lines indicate the absorbed dose rate without a range shifter.

TABLE 1 Measured absorbed dose rates and \bar{y}_D values for different irradiation settings.

Proton energy (MeV)	Irradiated target	AG (cm)	Position	Dose rate ($\mu\text{Gy/h}$)	\bar{y}_D ($\mu\text{Gy/h}$)
70	Phantom	NoRS	A	109.1 \pm 0.2	16.0 \pm 2.3
70	Phantom	10	A	51.8 \pm 0.2	37.9 \pm 4.0
70	Phantom	15	A	57.3 \pm 0.2	41.1 \pm 4.3
70	Phantom	23	A	59.1 \pm 0.2	38.1 \pm 4.1
70	Beam dump	NoRS	A	199.1 \pm 0.3	13.0 \pm 1.0
70	Beam dump	10	A	59.5 \pm 0.2	37.1 \pm 4.1
70	Beam dump	15	A	60.3 \pm 0.2	36.8 \pm 4.8
70	Beam dump	23	A	58.8 \pm 0.2	40.1 \pm 1.4
70	Phantom	NoRS	C	50.7 \pm 0.9	11.2 \pm 2.2
70	Phantom	10	C	29.1 \pm 0.8	14.8 \pm 3.8
70	Phantom	15	C	15.6 \pm 0.7	24.9 \pm 5.0
70	Phantom	23	C	22.0 \pm 0.7	28.4 \pm 4.9
70	Beam dump	NoRS	C	142.9 \pm 1.6	13.7 \pm 1.0
70	Beam dump	10	C	63.2 \pm 0.2	29.4 \pm 3.1
70	Beam dump	15	C	49.2 \pm 0.2	35.9 \pm 4.9
70	Beam dump	23	C	46.7 \pm 0.2	35.0 \pm 6.3
146	Phantom	NoRS	A	318.2 \pm 0.5	35.1 \pm 2.7
146	Phantom	10	A	1268 \pm 2.0	16.2 \pm 1.0
146	Phantom	15	A	2539 \pm 4.0	11.7 \pm 0.7
146	Phantom	23	A	2844 \pm 4.0	10.4 \pm 0.7
146	Beam dump	NoRS	A	496.0 \pm 0.7	24.8 \pm 1.5
146	Beam dump	10	A	2524.0 \pm 3.7	10.7 \pm 0.6
146	Beam dump	15	A	2678.3 \pm 3.9	10.8 \pm 0.6
146	Beam dump	23	A	2920.8 \pm 4.3	10.5 \pm 0.5
146	Phantom	NoRS	C	157.2 \pm 1.8	21.8 \pm 2.9
146	Phantom	10	C	128.6 \pm 1.5	33.9 \pm 2.4
146	Phantom	15	C	104.3 \pm 1.3	40.1 \pm 5.0
143	Phantom	23	C	116.5 \pm 1.4	35.2 \pm 4.1
146	Beam dump	NoRS	C	404.1 \pm 4.3	23.4 \pm 1.6
146	Beam dump	10	C	1448 \pm 15	12.9 \pm 0.9
146	Beam dump	15	C	1543 \pm 16	12.1 \pm 0.6
146	Beam dump	23	C	1723 \pm 18	10.3 \pm 0.8

Either the phantom or a proton beam dump was irradiated, and irradiations were made either with a range shifter at a certain range-shifter position (AG) or without the range shifter (NoRS). The values are given with two significant figures, and as mentioned in Section 2.4, the values are illustrated with statistical uncertainties only with $k = 1$. Effects from, e.g., uncertainties in gas pressure, detector dimensions, and the W value, give an additional contribution of 4%.

In the stray radiation field from the 70-MeV proton beam (Figures 4A, C), the absorbed dose decreased when applying a range shifter in both positions A and C, both with and without the presence of the phantom.

It is apparent that when the phantom was irradiated with a 146-MeV proton field (Figure 4B), the absorbed dose rate was dramatically increased in the A position when the range shifter was applied. The absorbed dose rate increased with the air gap. It is also notable that the dose rate when irradiated with a 146-MeV proton beam seemed to be independent of the presence of a phantom (Figure 4B vs. 4D) at 15- and 23-cm range-shifter positions, which is an indication that the majority of the dose contribution came from the range shifter. In the C position, which was shadowed by the phantom when it was present, the

dose rate decreased when the range shifter was applied. When irradiating without a range shifter and phantom, directly on the proton beam dump, it is noteworthy that the scattering from the range shifter was still higher than scattering from the beam dump.

3.2 Measured dose-mean lineal energy as a function of the range-shifter position

The covariance corrections in all measurements were small, confirming the stability of both the beam and the measurement system. This stability makes comparisons between \bar{y}_D values at the different range-shifter positions more reliable.

TABLE 2 Estimated H^* values for different irradiation settings.

Proton energy (MeV)	Irradiated target	AG (cm)	Position	H^* ($\mu\text{Sv/h}$)
70	Phantom	NoRS	A	377 \pm 43
70	Phantom	10	A	372 \pm 36
70	Phantom	15	A	442 \pm 42
70	Phantom	23	A	426 \pm 41
70	Beam dump	NoRS	A	586 \pm 33
70	Beam dump	10	A	418 \pm 42
70	Beam dump	15	A	421 \pm 50
70	Beam dump	23	A	452 \pm 44
146	Phantom	NoRS	A	2130 \pm 140
146	Phantom	10	A	4420 \pm 210
146	Phantom	15	A	6880 \pm 310
146	Phantom	23	A	7120 \pm 320
146	Beam dump	NoRS	A	2550 \pm 130
146	Beam dump	10	A	6430 \pm 240
146	Beam dump	15	A	6870 \pm 270
146	Beam dump	23	A	7350 \pm 250

Either the phantom or a proton beam dump was irradiated, and irradiations were made either with a range shifter at a certain range-shifter position (AG), or without the range shifter (NoRS). The values are given with two significant figures and as mentioned in Section 2.4, the values are illustrated with statistical uncertainties only with $k = 1$. Effects from, e.g., uncertainties in gas pressure, detector dimensions, and the W value give an additional contribution of 4%.

Figure 5 illustrates the \bar{y}_D values for different range-shifter settings, when both the phantom (Figures 5A, B) and the proton beam dump (Figures 5C, D) were irradiated. When the phantom was irradiated with 70-MeV protons, the \bar{y}_D values increased in both positions when a range shifter was inserted. In the A position, the \bar{y}_D value seemed to be independent of the range-shifter position, while there was an increasing trend in the C position. The increasing \bar{y}_D value indicates an increasing dose contribution from a high-LET component.

The most prominent results are seen in the right figures. When irradiating the phantom with a 146-MeV proton beam (Figure 5B), the \bar{y}_D value measured in the A position decreased from approximately 35 to 15 keV/ μm when applying the range shifter at a 10-cm air gap and then continued to decrease slightly with the increased air gap. The C side, being more shielded by the phantom, experienced the opposite—the \bar{y}_D value increased, but there was no significant air gap dependence. Compared to the 70-MeV proton irradiation (Figure 5A), the \bar{y}_D value at the C position increased, which can be explained by production of neutrons that were more highly energetic when irradiating with a 146-MeV proton beam than with a 70-MeV proton beam.

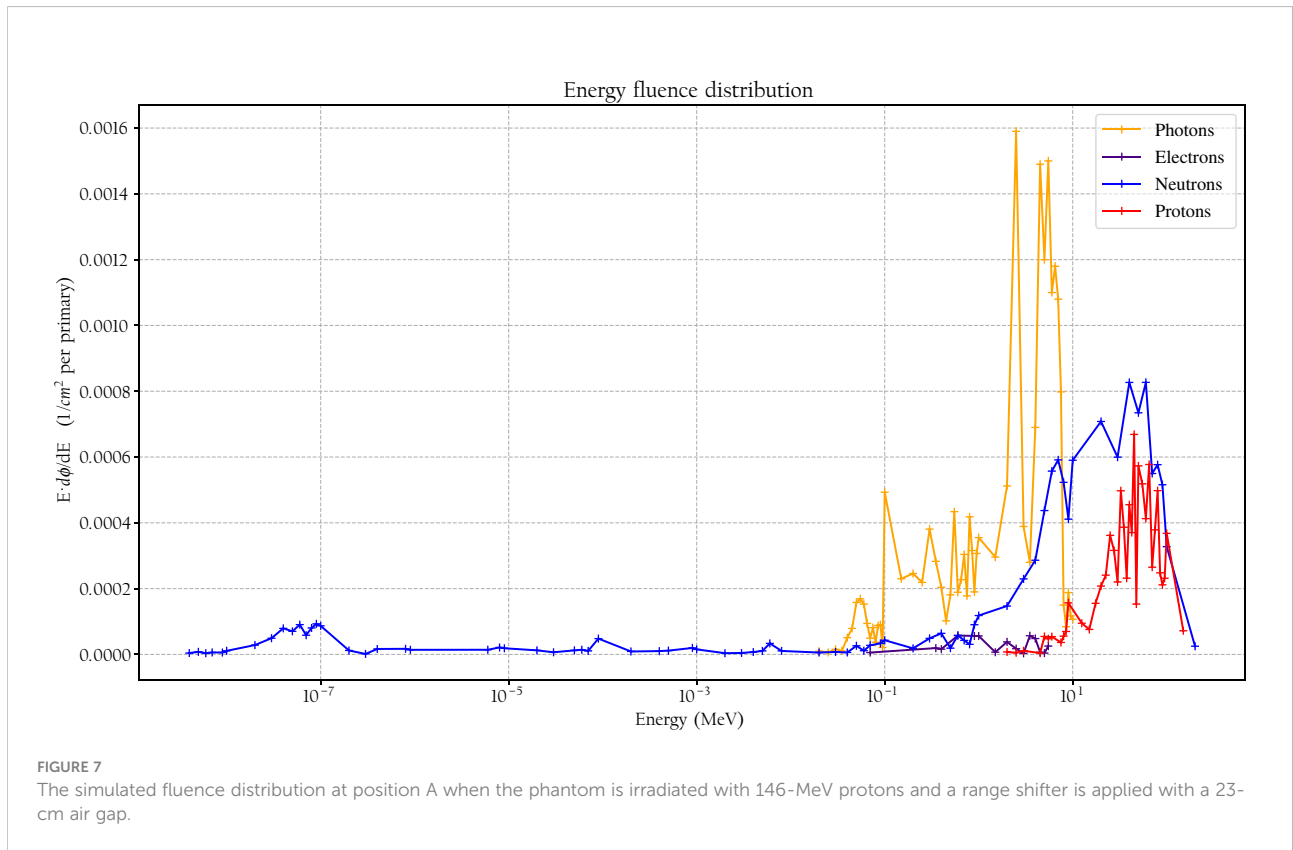
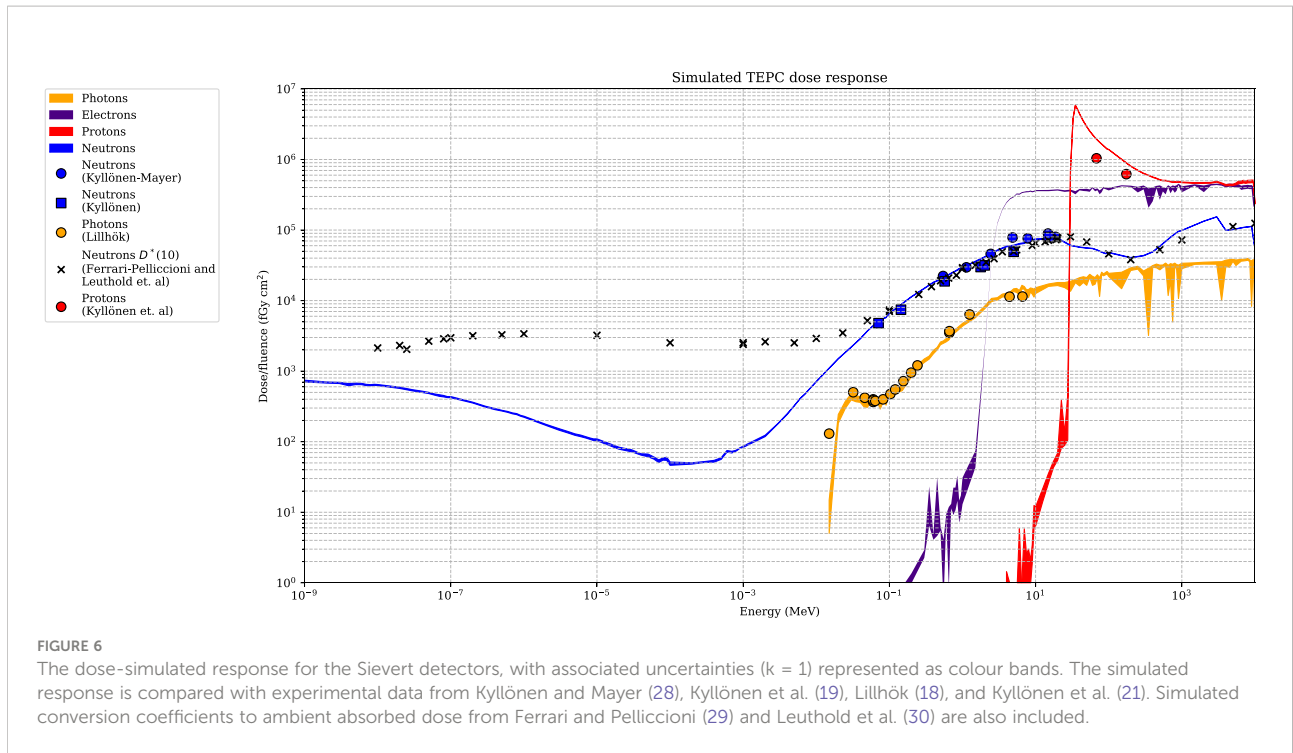
Figure 5D shows that when there was no phantom present, the \bar{y}_D value in both positions decreased, indicating a larger contribution of a low-LET component from the range shifter when irradiating with a 146-MeV proton beam.

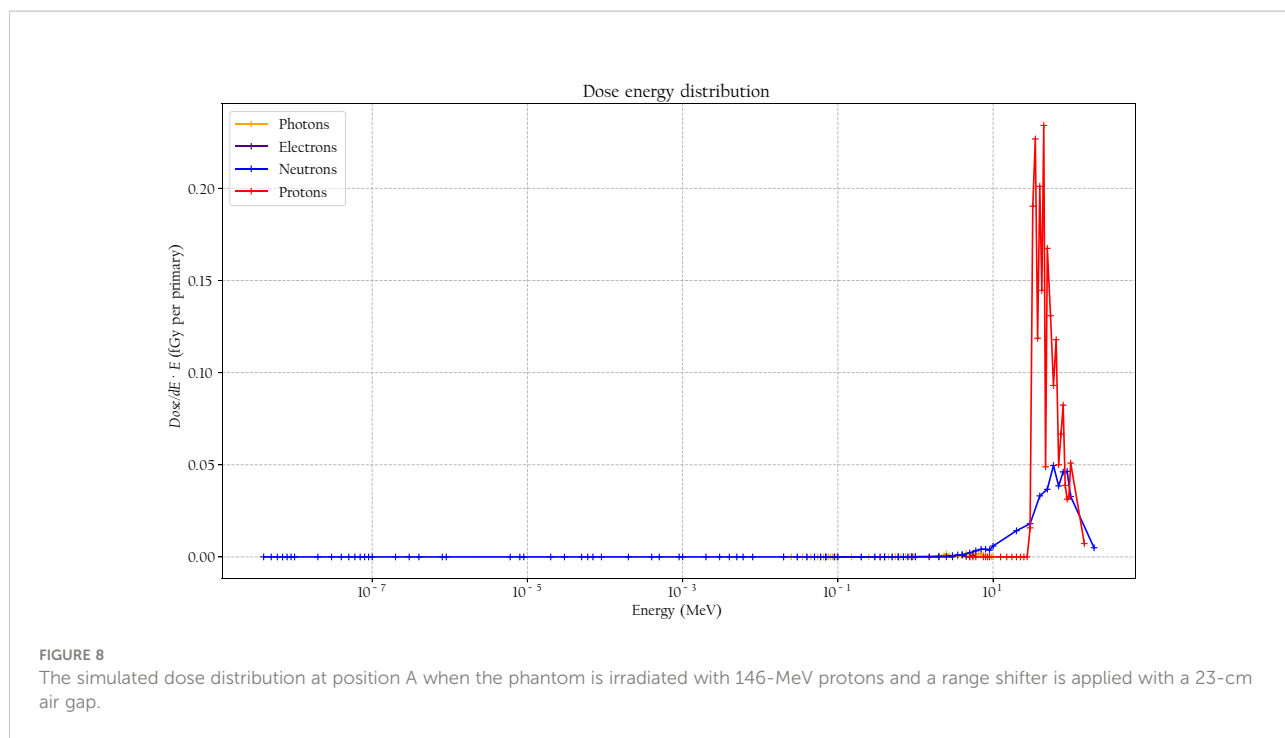
3.3 Simulated relative dose distributions

The simulated detector absorbed dose responses for neutrons, protons, photons, and electrons are presented in

Figure 6. Included are also measured values, using the same detectors, for neutrons, photons, and protons from Lillhök (18), Kyllönen et al. (19, 21), and Kyllönen and Mayer (28), as well as conversion coefficients to ambient absorbed doses from Ferrari and Pelliccioni (29) and Leuthold et al. (30). The conversion coefficients from Ferrari and Pelliccioni were calculated as the ratio of the reported H^* conversion coefficient and the effective quality factor at 10-mm depth in the ICRU sphere. A good agreement is seen between the simulated absorbed dose response and previously published experimental values for proton, neutrons, and photons. It can also be noted that the simulated detector absorbed dose and the ambient absorbed dose agree well for high neutron energies above 20 MeV where no experimental data were available. The energy-weighted fluence distributions at position A when the phantom is irradiated with a 146-MeV proton beam and the range shifter is applied at a 23-cm air gap are illustrated in Figure 7. The dose energy distribution for the same irradiation settings and position in Figure 8 shows that the dose deposited in the detector is mainly from > 10 -MeV protons.

In Figure 9, the simulated relative dose distributions from photons, neutrons, and protons are shown for the A position. When irradiating with a 70-MeV proton beam and using a range shifter, the majority of the dose is due to neutrons, as indicated by the increase in \bar{y}_D value seen in Figure 5A. During 146-MeV proton beam irradiations, the neutron contribution in position A decreases with increasing range-shifter position while the proton contribution increases sharply. At 15 and 23 cm, the relative contributions from the radiation components does not change significantly. We note here that also the \bar{y}_D value was relatively



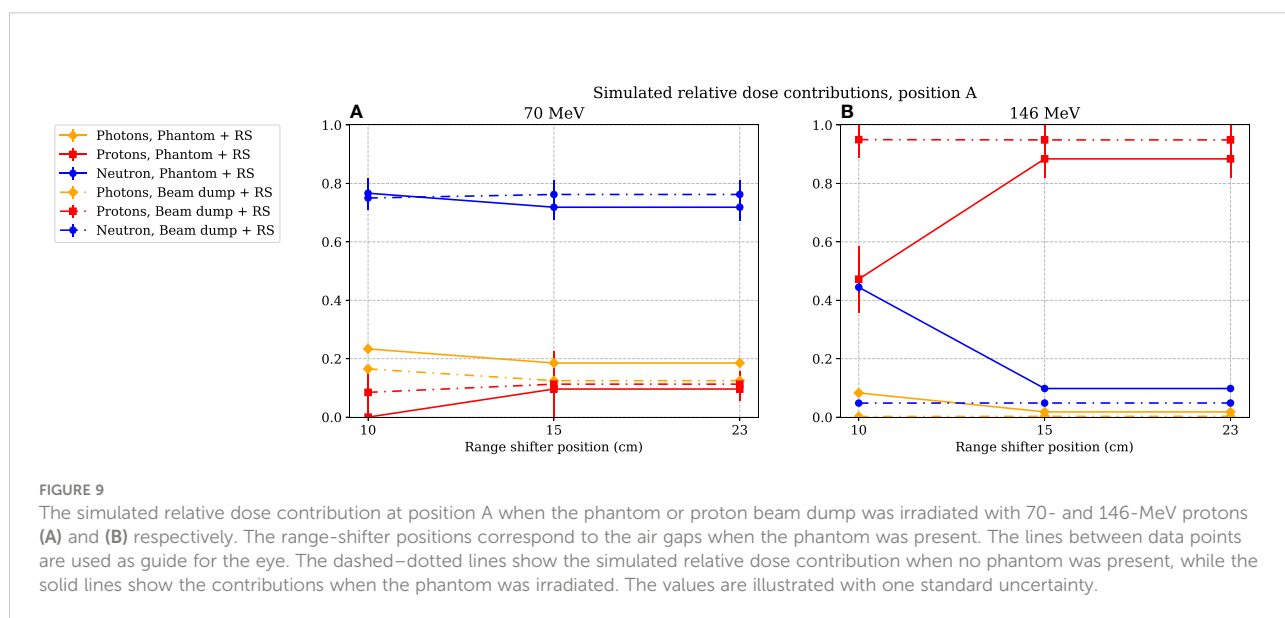


constant when comparing the 15- and 23-cm range-shifter positions (see Figure 5B).

The simulations were performed with a simple geometry, only including the detector, range shifter, phantom, and proton beam dump. To investigate the scattering effect of the surrounding structure, more thorough and hence time-consuming simulations were performed for a few cases, using a more comprehensive geometry modelled by Ardenfors et al. (27). These simulations showed that the surrounding walls were

important when relatively lowly absorbed doses were measured, particularly in position C, where the range shifter was shielded by the phantom. These complementary simulations did not change the conclusion that the primary beam was scattered in the range shifter. In position A, the increased absorbed dose was still completely dominated by the relative contribution of the scattered protons deposited in the detector.

From the simulated dose distribution, it is also evident that the contribution from photons is very low (see Figure 9), so any



low-LET components leading to a decrease in the resulting \bar{y}_D value at 146 MeV were likely to come from protons.

3.4 Estimated dose equivalent as a function of the range-shifter position

As for the simulated dose contributions, only the investigation of position A is presented here. The dose equivalents as functions of different range-shifter settings were estimated during irradiations of both the phantom and the proton beam dump (see Figure 10). In Figure 10A, for the 70-MeV proton beam, it is seen that the H^* values were relatively constant even after applying a range shifter. The absorbed dose rate was lower, and the increase of high-LET neutrons was not high enough to give a higher H^* value. During irradiation with a 146-MeV proton beam, two noteworthy results can be pointed out. First, the H^* value without a range shifter was higher than when irradiating with a 70-MeV proton beam, indicating that the stray field from the phantom alone led to an increase with an increased proton beam energy. This increase is expected since the proton energy was more than double. Second, when applying the range shifter, the H^* values increased by almost a factor of 2 (for the smallest range-shifter position when irradiating the phantom), up to a factor more than 3 (23-cm air gap). At the 10-cm air gap, position A was partly shadowed by the phantom, which explains the air gap dependence. The increase in the H^* value here reflects the significantly higher absorbed doses by the scattered protons.

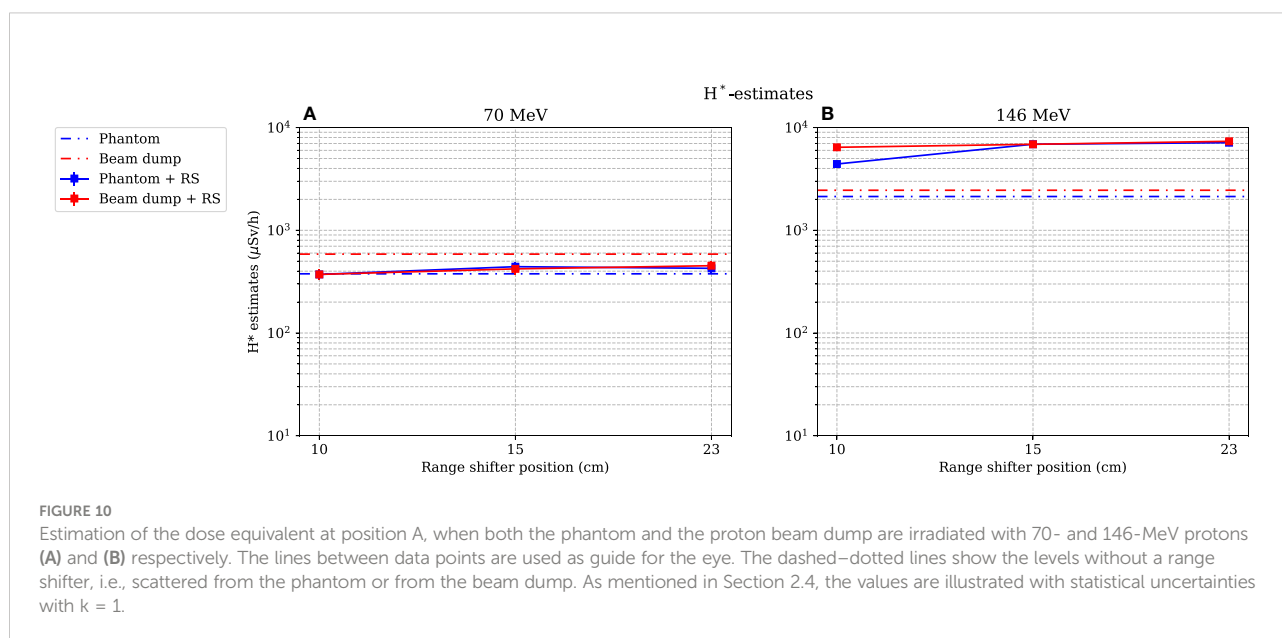
4 Discussion

When irradiating the phantom with 70-MeV protons, the absorbed dose rate at both positions A and C decreased and the

\bar{y}_D value increased when applying the range shifter, indicating a larger contribution from a high-LET component. In position C, an air gap dependency which was not seen in position A was noticed. The detected neutrons in position A were less moderated by the phantom even at small air gaps, while the neutrons that reached position C had a larger moderation due to more phantom material to penetrate. At larger air gaps, the exposed phantom material was reduced and the neutrons deposited were therefore more energetic. This is visualised in Figure 11, where the blue cones indicate the line of sight from the centre of the range shifter to the detectors at positions A and C. At larger air gaps, a particle travelling in a straight line from the range shifter to a detector passes through less phantom material than at smaller air gaps.

When the phantom was irradiated with 146-MeV protons, the absorbed dose rate in position A was significantly increased, which can be explained by protons scattering at a large enough angle from the range shifter to miss the phantom. A clear dependency on the air gap was observed. When the air gap was small, the phantom shadowed the detector, while at larger air gaps, the detector saw almost no effect from the phantom. The hypothesis that high-energy (>10-MeV) protons represent the main part of the dose contribution in the detector at position A is supported by the measured decrease in the \bar{y}_D value when the range shifter is applied, indicating a large contribution from a low-LET component. The simulated dose contributions agreed with the measurements and also indicated that contribution from photons was low, which further supports the hypothesis that the majority of the low-LET component comes from protons.

The H^* value is an approximation of the ambient dose equivalent, $H^*(10)$, and was calculated using a linear approximation. The differences between the ICRP Q value and



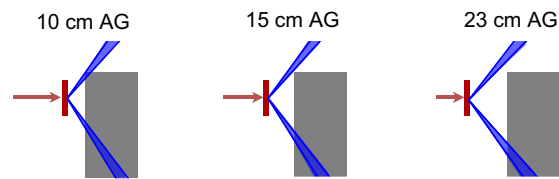


FIGURE 11

The blue cones indicate the path from the centre of the range shifter (red) to the borders of the detectors at positions A (top) and C (bottom). When the air gap is small, a particle that travels in a straight line needs to travel through more phantom material (grey) than when the air gap is large. This can be one reason to the air gap dependency that is seen for position C in Figure 5A.

this approximation is a source of uncertainty. In addition, e.g., back-scattering from the tissue material in the ICRU sphere was not detected in gas-filled TEPCs such as the Sievert detectors. Therefore, the absorbed dose from neutrons at intermediate energies is underestimated. An uncertainty of around 15%–25% has been estimated due to the abovementioned effects by Lillhök (18). The estimated H^* value during irradiations with 146-MeV protons was however several times larger with a range shifter than without and clearly exceeded the uncertainties in the ambient dose equivalent estimation even if the neutron energy distribution would change.

It is well established that the stray field in proton therapy contains both thermal and high-energy *neutron* components and that the magnitude of the contributions depends strongly on positions and proton beam energies (2, 4, 5). However, when applying a range shifter, the contributions at some positions that are less shielded by the phantom are not necessarily dominated by neutrons, and the thermal neutron contribution can be suppressed, as illustrated in Figures 7, 8. The range shifter can dramatically affect the stray radiation field. The potential presence of protons needs to be considered and included in simulations and measurements.

5 Conclusion

In a previous campaign, measuring the out-of-field neutron doses in a proton pencil beam facility, a significant increase in absorbed dose measured by a TEPC was detected at one position when a range shifter was applied. The measurements in the present study reproduced this increase, and measurements of the dose-mean lineal energy confirmed that the increased dose rate during irradiation with a 146-MeV proton beam consisted of low-LET radiation. The results were supported by Monte Carlo simulations showing that the low-LET component consisted of high-energy (>10-MeV) protons. The greatly enhanced dose rate when using the range shifter resulted in an up to three times higher dose equivalent compared to when no range shifter was applied. The results illustrate the importance of considering the potential dose contribution from protons in out-of-field

simulations as well as using instruments sensitive also to proton radiation during measurement campaigns.

Data availability statement

The raw data supporting the conclusions of this article will be made available by the authors, without undue reservation.

Author contributions

LE, JL, and TB planned the experimental measurements. RB-M performed the simulations. AD and ML planned and performed the irradiations at the Skandion Clinic. LE and JL performed pre-calibrations and preparations of the instruments. LE, JL, AD, and ML performed the measurements. LE performed the data analysis. LE did the main part of the writing and made the figures. All authors contributed to the article and approved the submitted version.

Funding

This project was funded by the Swedish Radiation Safety Authority, grant agreement no. 7030265-00. In addition, funding was received from Euratom's research and innovation programme 2019-20 under grant agreement no. 945196.

Acknowledgments

The authors would like to thank Oscar Ardenfors for providing a simulation geometry model for the Skandion treatment room. The Swedish National Metrology Laboratory for Ionising Radiation provided radioactive sources and equipment for control measurements and are gratefully acknowledged.

Conflict of interest

The authors declare that the research was conducted in the absence of any commercial or financial relationships that could be construed as a potential conflict of interest.

Publisher's note

All claims expressed in this article are solely those of the authors and do not necessarily represent those of their affiliated

organizations, or those of the publisher, the editors and the reviewers. Any product that may be evaluated in this article, or claim that may be made by its manufacturer, is not guaranteed or endorsed by the publisher.

References

- Smith AR. Vision 20/20 : Proton therapy. *Med Phys (Lancaster)* (2009) 36:556–68. doi: 10.1118/1.3058485
- Van Hoey O, Stolarczyk L, Lillhök J, Eliasson L, Mojżeszek N, Liszka M, et al. Simulation and experimental verification of ambient neutron doses in a pencil beam scanning proton therapy room as a function of treatment plan parameters. *Front Oncol* (2022) Submitted.
- ICRP. The 2007 recommendations of the international commission on radiological protection. *ICRP Publication 103. Ann. ICRP* (2007) 37:(2–4). doi: 10.1016/j.icrp.2007.10.003
- Farah J, Mares V, Romero-Expósito M, Trinkl S, Domingo D, Dufek V, et al. Measurement of stray radiation within a scanning proton therapy facility: EURADOS WG9 intercomparison exercise of active dosimetry systems. *Med Phys (Lancaster)* (2015) 42:2572–84. doi: 10.1118/1.4916667
- Trinkl S, Mares V, Englbrecht FS, Wilkens JJ, Wielunski M, Parodi K, et al. Systematic out-of-field secondary neutron spectrometry and dosimetry in pencil beam scanning proton therapy. *Med Phys (Lancaster)* (2017) 44:1912–20. doi: 10.1002/mp.12206
- Wochnik A, Stolarczyk L, Ambrozová, Davidkova M, De Saint-Hubert M, Dománski S, et al. Out-of-field doses for scanning proton radiotherapy of shallowly located paediatric tumours—a comparison. *Med Biol* (2021) 66(3):350123. doi: 10.1088/1361-6560/abcb1f
- ICRU. International Commission on Radiation Units and Measurements, Quantities and units in radiation protection dosimetry. *ICRU Report*. (1993) (ICRU, 7910 Woodmont Avenue, Suite 800: Bethesda, MD 208141) 51. doi: 10.1093/jicru_os26.2.15
- ICRU. International Commission on Radiation Units and Measurements, Determination of operational dose equivalent quantities for neutrons. *ICRU Report* (2001) (ICRU, 7910 Woodmont Avenue, Suite 800: Bethesda, MD 208141) 66. doi: 10.1093/jicru_1.3.3
- ICRU. International Commission on Radiation Units and Measurements, Microdosimetry. *ICRU Report 36* (1983) 36 (ICRU, 7910 Woodmont Avenue, Suite 800: Bethesda, MD 208141). doi: 10.1093/jicru_os19.1.80
- Kellerer AM, Rossi HH. On the determination of microdosimetric parameters in time-varying radiation fields: the variance-covariance method. *Radiat Res* (1984) 97:237–45. doi: 10.2307/3576275
- Lillhök J, Persson L, Andersen CE, Dasu A, Ardenfors O. Radiation protection measurements with the variance-covariance method in the stray radiation fields from photon and proton therapy facilities. *Radiat Prot Dosimetry* (2018) 180:338–41. doi: 10.1093/rpd/ncx194
- Kyllönen JE, Lindborg L, Samuelson G. Cosmic radiation measurements onboard aircraft with the variance method. *Radiat Prot Dosimetry* (2001) 93:197–205. doi: 10.1093/oxfordjournals.rpd.a006430
- Lillhök J, Beck P, Bottollier-Depois JF, Latocha M, Lindborg L, Roos H, et al. A comparison of ambient dose equivalent meters and dose calculations at constant flight conditions. *Radiat Meas* (2007) 42:323–33. doi: 10.1016/j.radmeas.2006.12.011
- Ambrozová I, Beck P, Benton ER, Billnert R, Bottollier-Depois JF, Caresana M, et al. REFLECT – research flight of EURADOS and CRREAT: Intercomparison of various radiation dosimeters onboard aircraft. *Radiat Meas* (2020) 137:106433. doi: 10.1016/j.radmeas.2020.106433
- Bolognese-Milsztajn T, Bartlett D, Boschung M, Coeck M, Curzio G, d'Errico F, et al. Individual neutron monitoring in workplaces with mixed neutron/photon radiation. *Radiat Prot Dosimetry* (2004) 110:753–8. doi: 10.1093/rpd/nch220
- Mayer S, Golnik N, Kyllönen JE, Menzel HG, Otto T. Dose equivalent measurements in a strongly pulsed high-energy radiation field. *Radiat Prot Dosimetry* (2004) 110:759–62. doi: 10.1093/rpd/nch177
- McConn R, Gesh CJ, Pagh RT, Rucker RA, Williams RGIII. *Compendium of material composition data for radiation transport modeling. PNNL-15870, rev. 1. tech. rep.* Richland, Washington: Pacific Northwest National Laboratory (2011).
- Lillhök JE. *The microdosimetric variance-covariance method used for beam quality characterization in radiation protection and radiation therapy.* (2007) Ph.D. thesis, Stockholm University, Medical Radiation Physics, Stockholm University, Karolinska Institutet.
- Kyllönen JE, Lindborg L, Samuelson G. The response of the sievert instrument in neutron beams up to 180 MeV. *Radiat Prot Dosimetry* (2001) 94:227–32. doi: 10.1093/oxfordjournals.rpd.a006494
- Vassiliev ON, Peterson CB, Cao W, Grosshans DR, Mohan R. Systematic microdosimetric data for protons of therapeutic energies calculated with Geant4-DNA. *Phys Med Biol* (2019) 64:215018–8. doi: 10.1088/1361-6560/ab47cc
- Kyllönen JE, Grindborg JE, Lindborg L. Response investigations of a TEPC in high energy proton and neutron beams using the variance method. *Radiat Prot Dosimetry* (2002) 99:373–4. doi: 10.1093/oxfordjournals.rpd.a006807
- ICRU. International Commission on Radiation Units and Measurements, Average energy required to produce an ion pair. *ICRU Report* (1979) 31 (ICRU, 7910 Woodmont Avenue, Suite 800: Bethesda, MD 208141). doi: 10.1093/jicru_os16.2.50
- Ardenfors O, Dasu A, Kopeć M, Gudowska I. Modelling of a proton spot scanning system using MCNP6. *J Phys Conf Ser* (2017) 860:12025. doi: 10.1088/1742-6596/860/1/012025
- Almhagen E, Boersma DJ, Nyström H, Ahnesjö A. A beam model for focused proton pencil beams. *Phys Med* (2018) 52:27–32. doi: 10.1016/j.ejmp.2018.06.007
- Christensen JB, Almhagen E, Stolarczyk L, Liszka M, Hernandez GG, Bassler N, et al. Mapping initial and general recombination in scanning proton pencil beams. *Phys Med Biol* (2020) 65:115003–3. doi: 10.1088/1361-6560/ab8579
- Werner CJ, Bull JS, Solomon CJ, Brown FB, McKinney GW, Rising ME, et al. *MCNP version 6.2 release notes. tech. rep.* United States: Los Alamos National Lab (2018). doi: 10.2172/1419730
- Ardenfors O, Dasu A, Lillhök J, Persson J, Gudowska I. Out-of-field doses from secondary radiation produced in proton therapy and the associated risk of radiation-induced cancer from a brain tumor treatment. *Phys Med* (2018) 53:129–36. doi: 10.1016/j.ejmp.2018.08.020
- Kyllönen JE, Mayer S. *Response investigations of the sievert instrument in neutron beams between 0.5 and 19 MeV at PTB.* Tech. rep.
- Ferrari A, Pelliccioni M. Fluence to dose equivalent conversion data and effective quality factors for high energy neutrons. *Radiat Prot Dosimetry* (1998) 76:215–224. doi: 10.1093/oxfordjournals.rpd.a032267
- Leuthild G, Mares V, Schraube H. Calculation of the neutron ambient dose equivalent on the basis of the ICRP revised quality factors. *Radiat Prot Dosimetry* (1992) 40:77–84. doi: 10.1093/oxfordjournals.rpd.a081194